THE JOURNAL OF PHYSICAL CHEMISTRY C

Article

Cite This: J. Phys. Chem. C 2019, 123, 9544−9551

pubs.acs.org/JPCC

Pervasive Cation Vacancies and Antisite Defects in Copper Indium Diselenide ($CuInSe_2$) Nanocrystals

Daniel W. Houck, Eli I. Assaf, Haein Shin, Randalynn M. Greene, Douglas R. Pernik, and Brian A. Korgel*

McKetta Department of Chemical Engineering and Texas Materials Institute, The University of Texas at Austin, Austin, Texas 78712, United States

Supporting Information

ABSTRACT: Copper indium diselenide ($CuInSe_2$) is a prototype ternary compound and group I−III−VI semiconductor with useful optoelectronic properties. $CuInSe_2$ nanocrystals have been of significant interest because of their size-tunable optical properties and lack of toxic heavy metals. Because of the particular vacancy and antisite substitutional point defects in $CuInSe_2$, large stoichiometric deviations can be tolerated, sometimes leading to the so-called ordered vacancy compounds (OVCs). Here, we use Raman spectroscopy of oleylamine-capped $CuInSe_2$ nanocrystals and ab initio lattice dynamics modeling to study the concentration and arrangements of ($2v_{Cu}^{-}$ + In_{Cu}^{2+}) defect pairs in the nanocrystals. The nanocrystals have randomly distributed defect pairs that become mobile under light excitation and accumulate, as in OVCs, along the [100] direction. Because the high concentration of vacancies in $CuInSe_2$ nanocrystals is compensated by In_{Cu}^{2+} antisite defects, these nanocrystals do not exhibit an optical plasmon resonance like many other copper chalcogenide nanocrystals. Annealing the nanocrystals at a high temperature (600 °C) was found to significantly reduce the defect concentration.

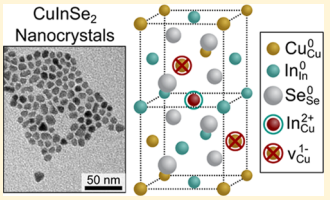

INTRODUCTION

There has been significant interest in colloidal nanocrystals of ternary compounds, especially group I−III−VI materials since they exhibit optical and optoelectronic properties similar to many II−VI and III−V semiconductors—but lack toxic elements like Cd, Pb or As—and could be potentially useful for a variety of applications, such as photovoltaic (PV) devices, luminescent glass and solar concentrators, and fluorescent contrast agents for biological imaging.[1−14] Copper indium diselenide ($CuInSe_2$) nanocrystals are a model for this class of materials.[15−20] Unlike ternary alloys, such as $Zn_xCd_{1-x}S$ or $CsPbI_xBr_{3-x}$, which have compositions that can be widely tuned, ternary compounds like $CuInSe_2$ exhibit preferred stoichiometry.[21−23] Even so, synthetic routes to $CuInSe_2$ nanocrystals often yield nanocrystals either enriched or depleted in In or Cu, with significant stoichiometric deviations from the ideal 1:1:2 molar ratio of Cu/In/Se.[17,19] $CuInSe_2$ tolerates these deviations because of the ready formation of copper vacancy and substitutional In antisite ($2v_{Cu}^{-}$ + In_{Cu}^{2+}) defect pairs.[2,23−25] In bulk films, the accumulation of these defects can give rise to ordered defect, or ordered vacancy, compounds (ODCs or OVCs), with stoichiometries like $CuIn_3Se_5$ and $CuIn_5Se_8$.[2,23−25] Colloidal nanocrystal quantum dots of I−III−VI OVCs have also been reported;[19] yet, little is actually known about these defects in $CuInSe_2$ nanocrystals and their stability.

Here, we use Raman spectroscopy to study the defects in $CuInSe_2$ nanocrystals capped with oleylamine (OLAm). With the aid of ab initio lattice dynamics calculations, Raman spectroscopy provides a way to determine the relative concentration and arrangement of ($2v_{Cu}^{-}$ + In_{Cu}^{2+}) defect pairs in the nanocrystals. The concentration of defect pairs is found to be heavily dependent on the crystallization temperature used during the nanocrystal synthesis. The defects appear to be randomly arranged in the as-synthesized nanocrystals but migrate into ordered arrangements like those in OVCs under light excitation. Thermal annealing at 600 °C greatly reduces the defect concentration and significantly enriches the concentration of In on the surface. These results show that the concentration of point defects in nanocrystals—and their interactions—can be very sensitive to the synthesis and processing conditions of the material. This is particularly important for optoelectronic applications like PVs, in which defects directly influence the properties of the material and device performance.

EXPERIMENTAL DETAILS

Chemicals. Copper(I) chloride (CuCl, 99.99%), indium chloride ($InCl_3$, 99.99%), selenium powder (Se, 100 mesh, 99.99%), anhydrous toluene (99.8%), oleylamine (OLAm, ≥98%), anhydrous tetrachloroethylene (TCE, ≥99%), and 70 wt % nitric acid (HNO_3) were purchased from Sigma-Aldrich. Copper, indium, and selenium standards (1 mg/mL) for inductively coupled plasma experiments were also purchased from Sigma-Aldrich. Toluene and ethanol were purchased from Fisher Scientific. OLAm was degassed before use by maintaining vacuum under 200 mTorr for 4 h at 110 °C and

Received: January 18, 2019
Revised: March 7, 2019
Published: March 11, 2019

DOI: 10.1021/acs.jpcc.9b00558
J. Phys. Chem. C 2019, 123, 9544−9551

then stored in a nitrogen-filled glovebox. All other chemicals were used as received.

$CuInSe_2$ Nanocrystal Synthesis. In a N_2-filled glovebox, 40 mL OLAm, 5 mmol (0.49 g) CuCl, 5 mmol (1.11 g) $InCl_3$, and 10 mmol (0.79 g) Se were added to a 100 mL three-neck flask. The flask was sealed with septa, removed from the glovebox, and transferred to a Schlenk line. The reaction mixture was heated to 110 °C under vacuum (<200 mTorr) for 1 h and then for 12 h under N_2 to allow the precursor complexes to completely form. The flask was heated to reaction temperatures of 180, 210, or 240 °C for 10 min. The heating mantle was then removed to allow the reaction mixture to cool down to room temperature. $CuInSe_2$ nanocrystals were purified by antisolvent precipitation by adding 20 mL of ethanol, followed by centrifugation at 2600 rcf for 5 min. After discarding the supernatant, the nanocrystals were redispersed in 10 mL of toluene and centrifuged again at 2600 rcf to remove poorly capped nanocrystals. The supernatant was transferred to another centrifuge tube, and one more antisolvent precipitation steps was carried out. Ethanol (4 mL) was added, followed by centrifugation at 2600 rcf for 5 min, and the supernatant was discarded. The product yields of dispersible OLAm-capped $CuInSe_2$ nanocrystals from reactions carried out at 180, 210, and 240 °C were 1.2 g (64%), 1.5 g (80%), and 1.3 g (70%), respectively. The nanocrystals were dispersed in anhydrous toluene and stored in a nitrogen-filled glovebox. The $CuInSe_2$ nanocrystals lose colloidal stability after a few days when exposed to air, but remain dispersed for months when stored in the glovebox.

Thermal Annealing of $CuInSe_2$ Nanocrystals. For some experiments, the nanocrystals were thermally annealed on Mo-coated soda lime glass substrates in an MTI OTF-1200X-RTP furnace. The furnace was held under vacuum (100 mTorr) for 10 min and then purged with nitrogen for 10 min. The chamber was then heated to 600 °C at 60 °C/min, held at 600 °C for 30 min, and then cooled down to room temperature.

Materials Characterization. Powder X-ray diffraction (XRD) data were acquired using a Rigaku R-axis Spider Diffractometer with an image plate detector. Cu Kα (λ = 1.54 Å) radiation was used with 40 kV and 40 mA power supply. Dried powder is suspended in a 0.5 mm nylon loop. The samples are scanned for 10 min while rotating at 1°/s. The diffraction patterns are integrated with the Rigaku 2DP powder processing program.

Samples for transmission electron microscopy (TEM) were prepared by drop-casting dilute nanocrystal solutions in toluene onto carbon film mesh nickel TEM grids purchased from Electron Microscopy Sciences. TEM images were obtained using an FEI Tecnai Spirit Bio Twin operated at 80 kV accelerating voltage.

Raman spectra were obtained using a Witec Micro-Raman Spectrometer α 300 with laser excitation at 488 nm. $CuInSe_2$ nanocrystals were deposited on Mo-coated 1/2″ × 1/2″ soda lime glass substrates by spin-coating 100 mg/mL dispersions in toluene. The $CuInSe_2$ films were about 150 nm thick according to contact profilometry. Changes in the Raman signal during the measurement due to laser exposure were avoided by acquiring the Raman signal immediately after the sample was exposed to the laser. Raman spectra were acquired for 5 s. For the time series measurements, Raman spectra were acquired for 5 s, followed by a 10 s delay in spectra acquisition while the sample remained illuminated by the laser.

Inductively coupled plasma atomic emission spectroscopy (ICP-AES) was performed with a Varian 710 ICP-AES. About 8 mg of nanocrystal sample was dissolved in 1 mL of 70% v/v nitric acid followed by dilution with DI-H_2O to a final concentration of 8 mg/L. The Cu 213.598, In 230.606, and Se 196.026 nm wavelength lines were used for the ICP-AES analysis, as these gave the lowest deviation between replicates. The reported error is the standard deviation of three replicates.

Absorbance spectra were measured with a Cary-5000 UV−Vis−NIR spectrophotometer. $CuInSe_2$ nanocrystals were dispersed in TCE and studied in quartz cuvettes with 1 cm path length. All spectra were background-subtracted against the same quartz cuvette filled with pure TCE.

X-ray photoelectron spectroscopy (XPS) was carried out with a Kratos Axis Ultra DLD photoelectron spectrophotometer using a monochromatic Al Kα X-ray source. Samples were prepared by spin-coating 100 mg/mL $CuInSe_2$ nanocrystal dispersions in toluene onto Mo-coated 1/2″ × 1/2″ soda lime glass substrates. The acquired spectra were processed using CasaXPS software. The charge on the samples was corrected by shifting the C 1s peak to 284.8 eV—the expected value for adventitious carbon (the Cu 1s XPS peaks are shown in the Supporting Information). Compositional estimates were calculated by fitting the peaks to a Gaussian−Lorentzian distribution and a Shirley background function. The peak area was then divided by the corresponding relative sensitivity factor and normalized to yield the surface-sensitive composition relative to Se.

Computational Methods. Raman spectra were performed using ab initio lattice dynamics calculations[26] similar to those described by Skelton et al.[27,28] Atomic positions of chalcopyrite $CuInSe_2$ were taken from the Pearson Crystallographic Database (ICSD: 73351, Pearson Symbol TL16).[29] PyCIFRW was used to generate the crystallographic information files (CIFs).[30] Structures are built containing 216 $CuInSe_2$ unit cells in a 6 × 6 × 6 configuration. Only phonons at the Γ-point of the structure were investigated, but by using a relatively large super-cell structure, the forces applied by neighboring atoms are accounted for and phonon modes near the edge of the unit cell Brillouin zone were explored. This method is described in detail by Qian et al.[31] Defect pairs (described by Zunger et al.[24,25]) defined by an In antisite in the (1/2, 1/2, 1/2) Cu site and vacancies in the (1/2, 0, 3/4) and (1, 1/2, 1/4) Cu sites are then added to various unit cells. Density functional theory (DFT) calculations[32−36] and density functional perturbation theory (DFPT)[37−40] calculations were carried out with the ABINIT software package and the AbiPy Python library.[41−43] The ground-state structure was determined through DFT calculations by varying the atomic positions to minimize the magnitude of the forces on the ions.[27,28,34,36] The magnitude of the forces was below 1 meV/Å in all ground-state structures. The Born effective charges and interatomic force constants were determined using DFPT calculations.[37−40] The phonopy and phonopy−spectroscopy code packages were then used to calculate dielectric tensors, determine Raman active phonon modes, and generate Raman spectra.[44−47] All DFT and DFPT calculations were carried out with a plane energy cutoff of 600 eV and a Γ-centered k-point spacing of 0.2 $Å^{-1}$. The generalized gradient approximation exchange−correlation functional of Perdew, Burke, and Ernzerhof, revised for solids (GGA-PBEsol), was used for the density functional interaction potentials.[48] The Cu.GGA_PBE, In.GGA_PBE, and Se.GGA_PBE atomic

DOI: 10.1021/acs.jpcc.9b00558
J. Phys. Chem. C 2019, 123, 9544−9551

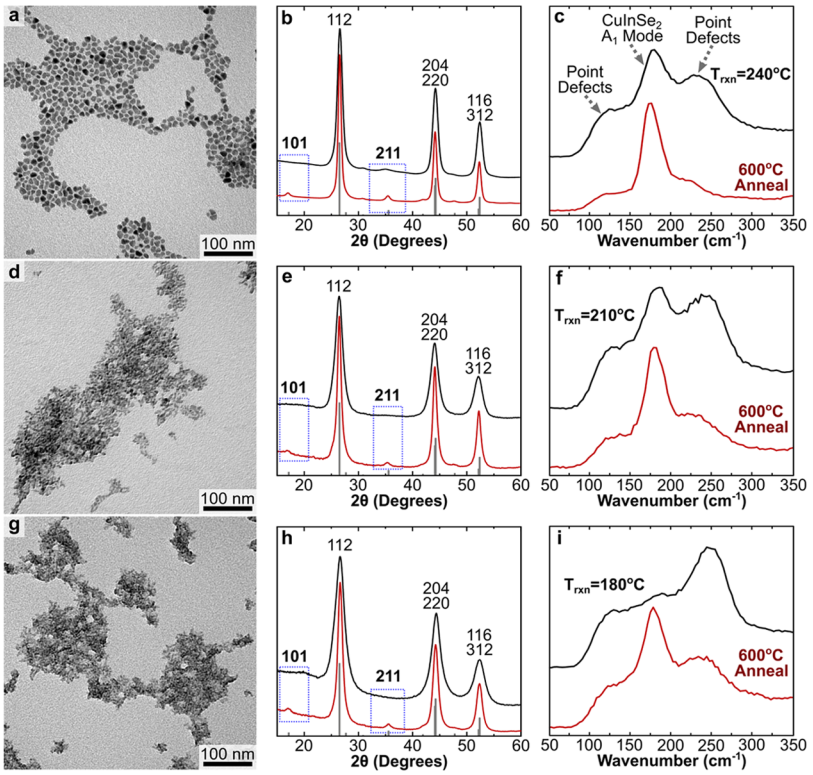

Figure 1. TEM, XRD, and Raman spectra of OLAm-capped $CuInSe_2$ nanocrystals obtained using three reaction temperatures: (a–c) 240 °C, (d–f) 210 °C, and (g–i) 180 °C. The average diameters of the nanocrystals in (a), (d), and (g) are 10.9 ± 2.3 nm, 5.2 ± 1.2 nm, and 3.4 ± 0.8 nm, respectively. The black and red curves (XRD and Raman spectra) correspond to nanocrystals before and after annealing under N_2 at 600 °C for 30 min, respectively. The XRD indexing corresponds to JCPDS no. 00-040-1487 for chalcopyrite $CuInSe_2$ (gray drop lines). Histograms of the nanocrystal size distributions and additional TEM images are provided as the Supporting Information.

Table 1. Size and Elemental Composition of the $CuInSe_2$ Nanocrystals Used in This Study[a]

	nanocrystal stoichiometry			
reaction temperature (°C)	Cu	In	Se	diameter (nm)
240	0.94 ± 0.03	1.02 ± 0.03	2.00 ± 0.05	10.9 ± 2.3
210	0.77 ± 0.02	1.07 ± 0.03	2.00 ± 0.02	5.2 ± 1.2
180	0.59 ± 0.01	1.14 ± 0.03	2.00 ± 0.06	3.4 ± 0.8

[a]The average diameters and standard deviations were determined from TEM images of 300 nanocrystals. Elemental compositions were measured by ICP-AES. Histograms of the nanocrystal size distributions are provided in the Supporting Information.

pseudopotentials from the ABINIT database were used for Cu, In, and Se.[49] The phonopy and phonopy–spectroscopy calculations an interaction range of 10 Å. All calculations were carried out with periodic boundary conditions at 300 K. The phonon line widths were calculated with the Phono3py postprocessing software, which determines broadening based on the phonon mode lifetime, as described by Skelton et al.[28] and Togo et al.[46] The phonon modes and intensities output by the calculations and "stick spectra" that indicate the calculated Raman spectra prior to broadening effects are available in the Supporting Information. The calculated XRD patterns for all structures are calculated using the visualization for electronic and structural analysis (VESTA) software, using a Cu Kα (λ = 1.54 Å) X-ray source, and no spectral broadening are also available in the Supporting Information.[50]

RESULTS AND DISCUSSION

For this study, nanocrystals were synthesized by heating CuCl, $InCl_3$, and Se in OLAm at three different temperatures: 180, 210, or 240 °C.[14,17] We found that the extent of defects in $CuInSe_2$ nanocrystals depended strongly on the growth temperature. Maintaining similar reaction conditions to make the nanocrystals, different growth temperatures gave particles with a slightly different size. Figure 1 shows the TEM images of the nanocrystals used in the study. The nanocrystals have average diameters of 3.4 ± 0.8, 5.2 ± 1.2, and 10.9 ± 2.3 nm that increase with increasing reaction temperature. Figure 1 also shows the X-ray diffraction (XRD) data for the nanocrystals. All of the XRD patterns are consistent with chalcopyrite (tetragonal) $CuInSe_2$ crystal structure, except for the absence of the (typically weak) (211) and (101) diffraction peaks. The lack of the (211) and (101) diffraction peaks indicates cation disorder and point defects in the nanocrystals.[19] This is consistent with nonstoichiometric elemental compositions determined by inductively coupled plasma atomic emission spectroscopy (ICP-AES), as shown in Table 1. Nanocrystals made at the lowest reaction temperature (180 °C) lack a significant amount of Cu, with a Cu/In molar ratio of only 0.52. Nanocrystals made at 210 °C have a Cu/In ratio of 0.72, and nanocrystals made at 240 °C are nearly

DOI: 10.1021/acs.jpcc.9b00558
J. Phys. Chem. C 2019, 123, 9544–9551

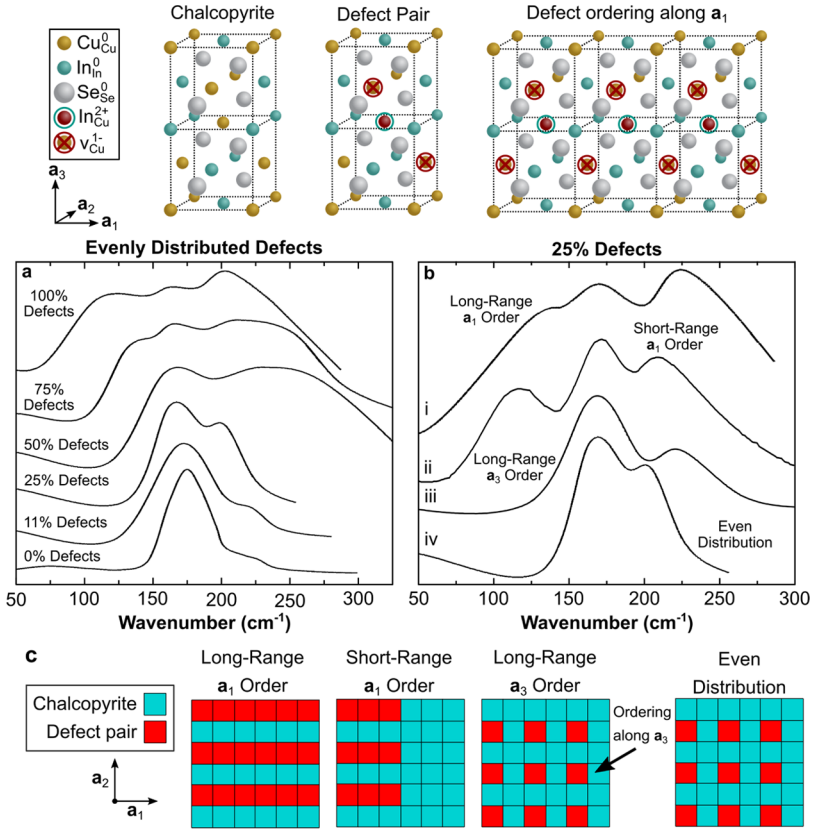

Figure 2. Raman spectra calculated for $CuInSe_2$ structures containing 216 unit cells. Defect pairs are defined by an In antisite defect in the (1/2, 1/2, 1/2) Cu site and Cu vacancies in the (1/2, 0, 3/4) and (1, 1/2, 1/4) Cu sites. (a) Defects are placed evenly throughout the structure at concentrations chosen such that 11, 25, 50, 75, and 100% of the unit cells in the structure contain a defect. (b) Raman spectra calculated for chalcopyrite $CuInSe_2$ nanocrystals built with 216 unit cells in a 6 × 6 × 6 configuration containing 54 defect pairs (25% defects) with different distributions. (i) $CuInSe_2$ structure in which the entire rows of unit cells in the (100) direction contain a defect pair. (ii) $CuInSe_2$ structure in which the defect pairs accumulate along half of the (100) row (three defected unit cells followed by three chalcopyrite unit cells). (iii) $CuInSe_2$ structures in which the entire columns of unit cells along the (001) direction contain a defect pair. (iv) $CuInSe_2$ structure with evenly distributed defect pairs. (c) Characteristic plane of unit cells illustrating different types of defect distributions. The precise defect distribution used for each calculation is provided as Supporting Information.

stoichiometric (yet nonetheless, deficient in Cu). The Raman spectra reveal that the nanocrystals have a significant number of defects. As shown in Figure 1c,f,i, the Raman spectra exhibit a peak at 175 cm^{-1} due to the A_1 vibrational mode of chalcopyrite $CuInSe_2$,[51−53] with two additional broad peaks at 120 and 240 cm^{-1} corresponding to defect-related modes. Similarly, broad Raman features straddling the A_1 mode have been observed at 150 and 260 cm^{-1} in extremely Cu-poor polycrystalline $CuInSe_2$ films grown by a coevaporation process[54] and at 152 and 220 cm^{-1} in $CuInSe_2$ films prepared by annealing hydrazine-based precursor solutions.[55] The defect-related Raman peaks observed in Figure 1c,f,i are significantly more pronounced for the nanocrystals made at lower synthesis temperatures.

The Raman spectra were compared to ab initio lattice dynamics calculations,[26−28] using a model of 216 chalcopyrite unit cells[29] in a 6 × 6 × 6 configuration with periodic boundary conditions and defect pairs inserted throughout with an In antisite at the (1/2, 1/2, 1/2) Cu atomic position and vacancies in the (1/2, 0, 3/4) and (1, 1/2, 1/4) Cu atomic positions. Zunger and co-workers have shown that these defect pairs have an exceptionally low energy of formation.[24,25] The defect pairs are also believed to occur in high concentrations, associate and order to give rise to the OVCs,[56] although the structural details in the bulk films are still being studied.[23] In our case, we examined how the positions of the defects in the nanocrystals were expected to affect the Raman spectra. Figure 2a shows the Raman spectra calculated for chalcopyrite $CuInSe_2$ with various concentrations of evenly distributed defect pairs. Defect-free chalcopyrite $CuInSe_2$ exhibits a sharp Raman peak at 175 cm^{-1}. The introduction of defect pairs creates a broad shoulder between 200 and 300 cm^{-1}. When more than half of the unit cells in the crystal contain defects, a second broad peak appears between 100 and 150 cm^{-1}. Table 2 summarizes the Cu, In, and Se compositions and vacancy concentrations used to calculate the spectra in Figure 2.

The arrangement of the defect pairs was also found to affect the Raman spectra. Figure 2b shows the Raman spectra calculated with 25% of the unit cells in the chalcopyrite structure containing pair defects in different configurations. When the defect pairs order and accumulate in the [100] direction (Figure 2b,i,ii), the A_1 signal becomes much broader and the defect peaks become stronger than when the defects were evenly distributed or accumulated along the [001] direction. Long-range ordering along [100] (Figure 2b,ii) exhibits the most significant A_1 broadening and the highest defect peak intensity. The Raman peak between 100 and 150 cm^{-1} is only observed in structures with [100] ordering, whereas the Raman peak between 200 and 300 cm^{-1} is observed in all structures containing defect pairs. This indicates

DOI: 10.1021/acs.jpcc.9b00558
J. Phys. Chem. C 2019, 123, 9544−9551

Table 2. Composition and Vacancy (v) Concentration of the $CuInSe_2$ Structures Used To Calculate the Raman Spectra in Figure 3a

	nanocrystal stoichiometry (normalized to Se)			
fraction of unit cells with a defect pair (%)	Cu	In	Se	v
0	1.00	1.00	2.00	0.00
11	0.92	1.03	2.00	0.06
25	0.81	1.06	2.00	0.13
50	0.63	1.13	2.00	0.25
75	0.44	1.19	2.00	0.38
100	0.25	1.25	2.00	0.50

that the enhanced peak broadening and appearance of the Raman peak between 100 and 150 cm^{-1} are caused by chains of undercoordinated Se atoms created when the defect pairs accumulate along the [100] direction. The calculated Raman spectra for structures in which 50% of the unit cells in the chalcopyrite structure contain pair defects exhibit similar behavior and are available in the Supporting Information. Calculated XRD patterns for all structures (see the Supporting Information) also resemble the experimentally observed X-ray patterns for chalcopyrite $CuInSe_2$, differing only in the intensity and position of the low-intensity XRD reflections.

Annealing the $CuInSe_2$ nanocrystals at 600 °C under N_2 was found to significantly sharpen the A_1 peak, as shown in Figure 1c,f,i. The A_1 peak also shifts slightly closer to the expected value of 175 cm^{-1}, and the defect-related peak intensities were greatly reduced. This processing temperature is similar to what is commonly used to process polycrystalline $CuInSe_2$ films for PVs.[23] Annealing also sharpened the XRD peaks, as in Figure 1b,e,h, indicating that significant crystal grain growth occurred. Furthermore, the (211) diffraction peak is now evident. These observations further confirm that relatively low synthesis temperatures lead to significant concentration of point defects in the $CuInSe_2$ nanocrystals. Higher temperatures allow the cations to redistribute into more thermodynamically favorable positions, resulting in the appearance of the (211) and (101) XRD peaks and the sharpening of the A_1 Raman mode.

X-ray photoelectron spectroscopy (XPS) provides another measure of the composition of the nanocrystals, which is more sensitive to the surface than ICP-AES. Thermal annealing led to significant defect redistribution. It could also lead to a loss of material, such as Se outgassing, for example, and XPS could provide an indication of whether significant changes in the overall stoichiometry occurred. Figure 3 shows the XPS data for the $CuInSe_2$ nanocrystals synthesized at 240 °C before and after annealing at 600 °C. The XPS peak shapes and positions are in good agreement with those observed for polycrystalline $CuInSe_2$[57,58] and $CuInSe_2$ nanocrystals.[59] There was no indication of significant Se loss. The annealing process, however, did cause the relative intensity of the Cu 2p spectral features in XPS to drop by nearly half. Since the XPS signal is extremely surface-sensitive and decays exponentially with penetration depth,[60] this reduction in intensity suggests that annealing causes Cu vacancies to migrate to the surface of the film. The composition of the nanocrystals is also similar to that of the Cu-poor surfaces often observed in polycrystalline $CuInSe_2$.[23,61,62] The surface-sensitive composition is estimated for a flat homogeneous sample by fitting the XPS peaks to a Gaussian/Lorentzian distribution and a Shirley background function.[63] The peak area is then divided by the relative sensitivity factor provided in the Kratos Library to generate the surface-sensitive composition estimate presented in Table 3. XPS of the annealed nanocrystals also reveals a decrease in the carbon signal of 40%, indicating the loss of ligands during the heating process (see the Supporting Information).

Table 3. Surface-Sensitive Composition Estimates of $CuInSe_2$ Nanocrystal Films Measured by XPS Before and After Annealing under N_2 at 600 °C for 30 min[a]

	surface-sensitive nanocrystal composition (normalized to Se)		
	Cu	In	Se
as-synthesized	0.98	1.62	2.00
600 °C 30 min anneal	0.52	1.97	2.00

[a]Composition is estimated assuming a flat, homogeneous sample by dividing the integrated peak intensity by the corresponding relative sensitivity factor.

The Raman spectra were also found to shift over time, as the samples were exposed to the excitation laser, indicating that the defects in the $CuInSe_2$ nanocrystals are sensitive to light. As shown in Figure 4a, the relative intensity of the A_1 peak decreases significantly relative to the defect-related peaks after only seconds of exposure to the 1 mW, 488 nm, laser with an approximately 1 μm diameter spot size. In contrast, the Raman spectra in Figure 4b of nanocrystals annealed at 600 °C (under N_2) were completely stable under the excitation laser. Thermal

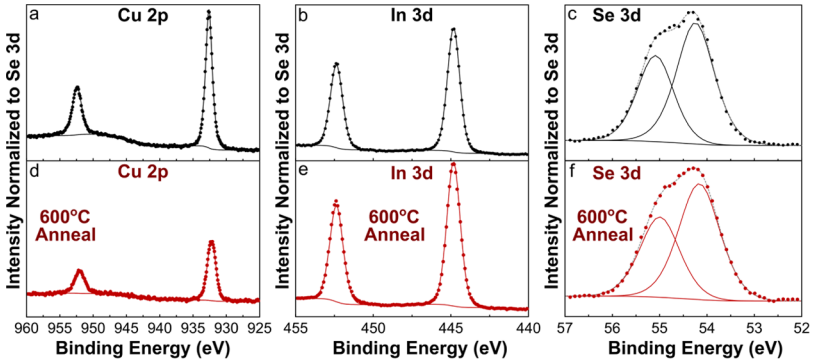

Figure 3. X-ray photoelectron spectra of the $CuInSe_2$ nanocrystals synthesized at 240 °C (a–c) before and (d–f) after annealing under N_2 at 600 °C for 30 min. The spectra are taken on the (a, d) Cu 2p, (b, e) In 3d, and (c, f) Se 3d spectral regions. The intensity of the Cu 2p and In 3d peaks is normalized to the maximum intensity of the Se 3d peak at 54.3 eV of the same sample.

DOI: 10.1021/acs.jpcc.9b00558
J. Phys. Chem. C 2019, 123, 9544–9551

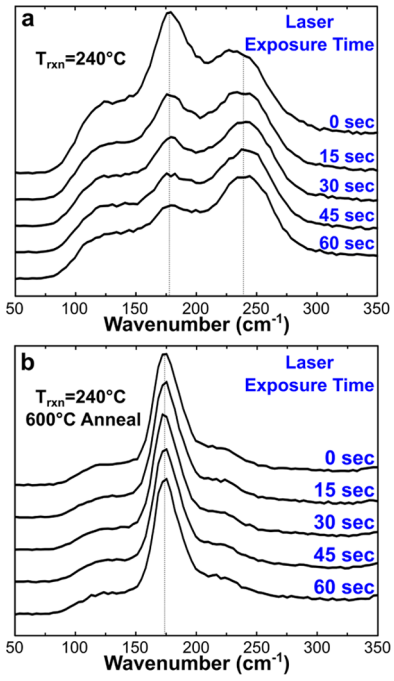

Figure 4. Evolution of the Raman spectra of $CuInSe_2$ nanocrystals synthesized at 240 °C during exposure to the Raman Laser (a) before and (b) after annealing under N_2 at 600 °C for 30 min. A 5 s acquisition time and a 10 s delay were used between acquisitions to generate the time series.

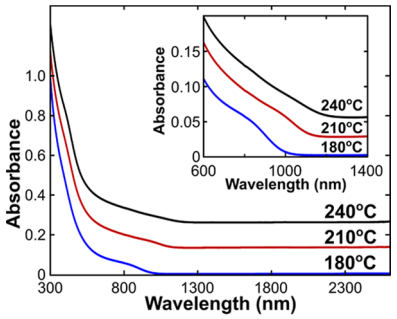

Figure 5. Room-temperature UV−vis−NIR absorbance spectra of OLAm-capped $CuInSe_2$ nanocrystals synthesized at 240, 210, and 180 °C dispersed in tetrachloroethylene (TCE). The average diameters of the nanocrystals are 10.9 ± 2.3, 5.2 ± 1.2, and 3.4 ± 0.8 nm, respectively. Note the absence of an NIR plasmon peak. The spectra are vertically offset for clarity. The inset shows the rescaled absorbance spectra to highlight the size dependence of the absorption onset.

annealing sharpens the A_1 feature, significantly reduces the defect-related Raman peaks, and greatly improves the stability of the Raman spectra under the excitation laser. Photoinduced defect mobility appears to be much greater in the as-synthesized nanocrystals than that in the nanocrystals after thermal annealing at 600 °C. The simulations indicate that illumination with the Raman excitation laser induces the migration and accumulation of the defect pairs in the (100) direction. The introduction of vacancies into CuS nanocrystals by laser excitation has also been reported.[64]

Cu vacancies in related Cu_xS and Cu_xSe nanocrystals lead to free carrier doping and resultant plasmonic optical responses at NIR wavelengths.[65,66] Cu vacancies are also present in relatively high concentrations in the Cu-deficient $CuInSe_2$ nanocrystals studied here, but because of charge-compensating antisite defects, there are no plasmon resonances observed in the optical absorbance spectra, as shown in Figure 5. The largest nanocrystals, with 10.9 nm average diameter, exhibit an absorption onset at 1250 nm, similar to the 1.01 eV band-to-band optical transition known for bulk polycrystalline $CuInSe_2$.[23,67] The absorption onsets of the 5.2 and 3.4 nm nanocrystals are blue-shifted due to quantum size effects, and the smallest nanocrystals exhibit a broad exciton feature.[68]

CONCLUSIONS

Raman spectroscopy and ab initio lattice dynamics calculations indicate that $CuInSe_2$ nanocrystals synthesized by arrested precipitation with OLAm-capping ligands contain a significant concentration of point defects, specifically copper vacancies and charge-compensating In_{Cu}^{2+} antisite defects. This is consistent with the absence of the (211) and (101) diffraction peaks in the XRD data and stoichiometry that is Cu poor and In rich. Lower synthesis temperatures led to significantly higher defect concentrations. Defects in the $CuInSe_2$ nanocrystals were also found to be very sensitive to exposure to the excitation laser, leading to a rapid increase in the intensity of the defect-related peaks, likely caused by the defect migration and accumulation of pair defects in the [100] direction. Annealing the nanocrystals at 600 °C significantly improved the crystallinity and decreased the defect concentration. After thermal annealing, the Raman spectra were largely unaffected by the excitation laser. Cu vacancies readily form in $CuInSe_2$ nanocrystals—similar to those in Cu_xS or Cu_xSe nanocrystals—however, charge-compensating antisite defects in $CuInSe_2$ prevent the appearance of optical plasmon features. It appears likely that this unique nature of the point defects in $CuInSe_2$ nanocrystals is largely responsible for making the material relatively robust for photovoltaic applications[12] compared to that of other types of semiconductor nanocrystals—similar to that of bulk[23,24] $CuInSe_2$—even with the relatively low synthesis temperatures and high concentrations of defects in the material.

ASSOCIATED CONTENT

Supporting Information

The Supporting Information is available free of charge on the ACS Publications website at DOI: 10.1021/acs.jpcc.9b00558.

Nanocrystal size distributions; TEM images; defect distributions used for Raman calculations; calculated Raman spectra for structures containing 50% defects in ordered distributions; calculated XRD patterns for all structures; XPS regions corresponding to the C 1s peaks; plots of calculated Raman frequencies and intensities with no spectral broadening; and Raman frequencies and intensities output from the Raman calculations (PDF)

AUTHOR INFORMATION

Corresponding Author

*E-mail: korgel@che.utexas.edu.

ORCID

Brian A. Korgel: 0000-0001-6242-7526

Notes

The authors declare no competing financial interest.

DOI: 10.1021/acs.jpcc.9b00558
J. Phys. Chem. C 2019, 123, 9544−9551

■ ACKNOWLEDGMENTS

The authors thank Hugo Celio for assistance with XPS. Financial support of this research was by the Robert A. Welch Foundation (F-1464) and the NSF Industry/University Cooperative Research Center on Next Generation Photovoltaics (IIP-1540028 and IIP-1822206).

■ REFERENCES

(1) Chen, B.; Pradhan, N.; Zhong, H. From Large-Scale Synthesis to Lighting Device Applications of Ternary I-III-VI Semiconductor Nanocrystals: Inspiring Greener Material Emitters. *J. Phys. Chem. Lett.* **2018**, *9*, 435−445.

(2) Yarema, O.; Yarema, M.; Wood, V. Tuning the Composition of Multicomponent Semiconductor Nanocrystals: The Case of I-III-VI Materials. *Chem. Mater.* **2018**, *30*, 1446−1461.

(3) Lauth, J.; Marbach, J.; Meyer, A.; Dogan, S.; Klinke, C.; Kornowski, A.; Weller, H. Virtually Bare Nanocrystal Surfaces: Significantly Enhanced Electrical Transport in $CuInSe_2$ and $CuIn_{1-x}Ga_xSe_2$ Thin Films upon Ligand Exchange with Thermally Degradable 1-Ethyl-5-Thiotetrazole. *Adv. Funct. Mater.* **2014**, *24*, 1081−1088.

(4) Singh, M.; Jiu, J.; Sugahara, T.; Suganuma, K. Thin-Film Copper Indium Gallium Selenide Solar Cells Based on Low-Temperature All-Printing Process. *ACS Appl. Mater. Interfaces* **2014**, *6*, 16297−16303.

(5) Sandroni, M.; Wegner, K. D.; Aldakov, D.; Reiss, P. Prospects of Chalcopyrite-Type Nanocrystals for Energy Applications. *ACS Energy Lett.* **2017**, *2*, 1076−1088.

(6) Pinchetti, V.; Lorenzon, M.; McDaniel, H.; Lorenzi, R.; Meinardi, F.; Klimov, V. I.; Brovelli, S. Spectro-electrochemical Probing of Intrinsic and Extrinsic Processes in Exciton Recombination in I-III-VI_2 Nanocrystals. *Nano Lett.* **2017**, *17*, 4508−4517.

(7) Nagamine, G.; Nunciaroni, H. B.; McDaniel, H.; Efros, A. L.; de Brito Cruz, C. H.; Padilha, L. A. Evidence of Band-Edge Hole Levels Inversion in Spherical $CuInS_2$ Quantum Dots. *Nano Lett.* **2018**, *18*, 6353−6359.

(8) McHugh, K. J.; Jing, L.; Behrens, A. M.; Jayawardena, S.; Tang, W.; Gao, M.; Langer, R.; Jaklenec, A. Biocompatible Semiconductor Quantum Dots as Cancer Imaging Agents. *Adv. Mater.* **2018**, *30*, No. 1706356.

(9) Cassette, E.; Pons, T.; Bouet, C.; Helle, M.; Bezdetnaya, L.; Marchal, F.; Dubertret, B. Synthesis and Characterization of Near-Infrared Cu-In-Se/ZnS Core/Shell Quantum Dots for In vivo Imaging. *Chem. Mater.* **2010**, *22*, 6117−6124.

(10) Panthani, M. G.; Khan, T. A.; Reid, D. K.; Hellebusch, D. J.; Rasch, M. R.; Maynard, J. A.; Korgel, B. A. In Vivo Whole Animal Fluorescence Imaging of a Microparticle-Based Oral Vaccine Containing $(CuInSe_xS_{2-x})$/ZnS Core/Shell Quantum Dots. *Nano Lett.* **2013**, *13*, 4294−4298.

(11) Meinardi, F.; McDaniel, H.; Carulli, F.; Colombo, A.; Valizhanin, K. A.; Makarov, N. S.; Simonutti, R.; Klimov, V. I.; Brovelli, S. Highly Efficient Large-Area Colourless, Luminescent Solar Concentrators Using Heavy-Metal-Free Colloidal Quantum Dots. *Nat. Nanotechnol.* **2015**, *10*, 878−885.

(12) Voggu, V. R.; Sham, J.; Pfeffer, S.; Pate, J.; Fillip, L.; Harvey, T. B.; Brown, R. M.; Korgel, B. A. Flexible $CuInSe_2$ Nanocrystal Solar Cells on Paper. *ACS Energy Lett.* **2017**, *2*, 574−581.

(13) Pernik, D. R.; Gutierrez, M.; Thomas, C.; Voggu, V. R.; Yu, Y.; van Embden, J.; Topping, A. J.; Jasieniak, J. J.; Vanden Bout, D. A.; Lewandowski, R.; Korgel, B. A. Plastic Microgroove Solar Cells Using $CuInSe_2$ Nanocrystals. *ACS Energy Lett.* **2016**, *1*, 1021−1027.

(14) Panthani, M. G.; Akhavan, V.; Goodfellow, B.; Schmidtke, J. P.; Dunn, L.; Dodabalapur, A.; Barbara, P. F.; Korgel, B. A. Synthesis of $CuInS_2$, $CuInSe_2$, and $Cu(In_xGa_{1-x})Se_2$ (CIGS) Nanocrystal "Inks" for Printable Photovoltaics. *J. Am. Chem. Soc.* **2008**, *130*, 16770−16777.

(15) Guo, Q.; Kim, S. J.; Kar, M.; Shafarman, W. N.; Birkmire, R. W.; Stach, E. A.; Agrawal, R.; Hillhouse, H. W. Development of $CuInSe_2$ Nanocrystal and Nanoring Inks for Low-Cost Solar Cells. *Nano Lett.* **2008**, *8*, 2982−2987.

(16) Tappan, B. A.; Barim, G.; Kwok, J. C.; Brutchey, R. L. Utilizing Diselenide Precursors toward Rationally Controlled Synthesis of Metastable $CuInSe_2$ Nanocrystals. *Chem. Mater.* **2018**, *30*, 5704−5713.

(17) Houck, D. W.; Korgel, B. A. Facile Exchange of Tightly Bonded L-Type Oleylamine and Diphenylphosphine Ligands on Copper Indium Diselenide Nanocrystals Mediated by Molecular Iodine. *Chem. Mater.* **2018**, *30*, 8359−8367.

(18) Zhong, H.; Wang, Z.; Bovero, E.; Lu, Z.; van Veggel, F. C. J. M.; Scholes, G. D. Colloidal $CuInSe_2$ Nanocrystals in the Quantum Confinement Regime: Synthesis, Optical Properties, and Electroluminescence. *J. Phys. Chem. C* **2011**, *115*, 12396−12402.

(19) Allen, P. M.; Bawendi, M. G. Ternary I-III-VI Quantum Dots Luminescent in the Red to Near-Infrared. *J. Am. Chem. Soc.* **2008**, *130*, 9240−9241.

(20) Coughlan, C.; Ibáñez, M.; Dobrozhan, O.; Singh, A.; Cabot, A.; Ryan, K. M. Compound Copper Chalcogenide Nanocrystals. *Chem. Rev.* **2017**, *117*, 5865−6109.

(21) Zhong, X.; Feng, Y.; Knoll, W.; Han, M. Alloyed $Zn_xCd_{1-x}S$ Nanocrystals with Highly Narrow Luminescence Spectral Width. *J. Am. Chem. Soc.* **2003**, *125*, 13559−13563.

(22) Nedelcu, G.; Protesescu, L.; Yakunin, S.; Bodnarchuk, M. I.; Grotevent, M. J.; Kovalenko, M. V. Fast Anion-Exchange in Highly Luminescent Nanocrystals of Cesium Lead Halide Perovskites ($CsPbX_3$, X = Cl, Br, I). *Nano Lett.* **2015**, *15*, 5635−5640.

(23) Stanbery, B. J. Copper Indium Selenides and Related Materials for Photovoltaic Devices. *Crit. Rev. Solid State Mater. Sci.* **2002**, *27*, 73−117.

(24) Zhang, S. B.; Wei, S.-H.; Zunger, A.; Katayama-Yoshida, H. Defect Physics of the $CuInSe_2$ Chalcopyrite Semiconductor. *Phys. Rev. B* **1998**, *57*, 9642−9656.

(25) Zhang, S. B.; Wei, S.-H.; Zunger, A. Stabilization of Ternary Compounds via Ordered Arrays of Defect Pairs. *Phys. Rev. Lett.* **1997**, *78*, 4059−4062.

(26) Ackland, G. J.; Warren, M. C.; Clark, S. J. Practical Methods in Ab Initio Lattice Dynamics. *J. Phys. Condens. Matter* **1997**, *9*, 7861−7872.

(27) Skelton, J. M.; Jackson, A. J.; Dimitrievska, M.; Wallace, S. K.; Walsh, A. Vibrational Spectra and Lattice Thermal Conductivity of Kesterite-Structured Cu_2ZnSnS_4 and $Cu_2ZnSnSe_4$. *APL Mater.* **2015**, *3*, No. 041102.

(28) Skelton, J. M.; Burton, L. A.; Jackson, A. J.; Oba, F.; Parker, S. C.; Walsh, A. Lattice Dynamics of the Tin Sulphides SnS_2, SnS and Sn_2S_3: Vibrational Spectra and Thermal Transport. *Phys. Chem. Chem. Phys.* **2017**, *19*, 12452−12465.

(29) Knight, K. S. The Crystal Structures of $CuInSe_2$ and $CuInTe_2$. *Mater. Res. Bull.* **1992**, *27*, 161−167.

(30) Hester, J. R. A Validating CIF Parser: PyCIFRW. *J. Appl. Crystallogr.* **2006**, *39*, 621−625.

(31) Qian, Q.; Zhang, Z.; Chen, K. J. In Situ Resonant Raman Spectroscopy to Monitor the Surface Functionalization of MoS_2 and WSe_2 for High-k Integration: A First-Principles Study. *Langmuir* **2018**, *34*, 2882−2889.

(32) Kresse, G.; Furthmüller, J. Efficiency of Ab-Initio Total Energy Calculations for Metals and Semiconductors Using a Plane-Wave Basis Set. *Comput. Mater. Sci.* **1996**, *6*, 15−50.

(33) Kresse, G.; Furthmüller, J. Efficient Iterative Schemes for *Ab Initio* Total-Energy Calculations Using a Plane-Wave Basis Set. *Phys. Rev. B* **1996**, *54*, 11169−11186.

(34) Kresse, G.; Hafner, J. Ab Initio Molecular Dynamics for Liquid Metals. *Phys. Rev. B* **1993**, *47*, 558−561.

(35) Kresse, G.; Joubert, D. From Ultrasoft Pseudopotentials to the Projector Augmented-Wave Method. *Phys. Rev. B* **1999**, *59*, 1758−1775.

(36) Blöchl, P. E. Projector Augmented-Wave Method. *Phys. Rev. B* **1994**, *50*, 17953−17979.

(37) Gajdoš, M.; Hummer, K.; Kresse, G.; Furthmüller, J.; Bechstedt, F. Linear Optical Properties in the Projector-Augmented Wave Methodology. *Phys. Rev. B* **2006**, *73*, No. 045112.

DOI: 10.1021/acs.jpcc.9b00558
J. Phys. Chem. C 2019, 123, 9544−9551

(38) Gonze, X. A Brief Introduction to the ABINIT Software Package. *Z. Kristallogr. - Cryst. Mater.* **2005**, *220*, 558−562.
(39) Gonze, X.; Lee, C. Dynamical Matrices, Born Effective Charges, Dielectric Permittivity Tensors, and Interatomic Force Constants from Density-Functional Perturbation Theory. *Phys. Rev. B* **1997**, *55*, 10355−10368.
(40) Baroni, S.; de Gironcoli, S.; Dal Corso, A.; Giannozzi, P. Phonons and Related Crystal Properties from Density-Functional Perturbation Theory. *Rev. Mod. Phys.* **2001**, *73*, 515−562.
(41) Gonze, X.; Beuken, J.-M.; Caracas, R.; Detraux, F.; Fuchs, M.; Rignanese, G.-M.; Sindic, L.; Verstraete, M.; Zerah, G.; Jollet, F.; et al. First-Principles Computation of Material Properties: The ABINIT Software Project. *Comput. Mater. Sci.* **2002**, *25*, 478−492.
(42) Gonze, X.; Jollet, F.; Abreu Araujo, F.; Adams, D.; Amadon, B.; Applencourt, T.; Audouze, C.; Beuken, J.-M.; Bieder, J.; Bokhanchuk, A.; et al. Recent Developments in the ABINIT Software Package. *Comput. Phys. Commun.* **2016**, *205*, 106−131.
(43) Gonze, X.; Amadon, B.; Anglade, P.-M.; Beuken, J.-M.; Bottin, F.; Boulanger, P.; Bruneval, F.; Caliste, D.; Caracas, R.; Côté, M.; et al. ABINIT: First-Principles Approach to Material and Nanosystem Properties. *Comput. Phys. Commun.* **2009**, *180*, 2582−2615.
(44) Togo, A.; Chaput, L.; Tanaka, I.; Hug, G. First-Principles Phonon Calculations of Thermal Expansion in Ti_3SiC_2, Ti_3AlC_2, and Ti_3GeC_2. *Phys. Rev. B* **2010**, *81*, No. 174301.
(45) Chaput, L.; Togo, A.; Tanaka, I.; Hug, G. Phonon-Phonon Interactions in Transition Metals. *Phys. Rev. B* **2011**, *84*, No. 094302.
(46) Togo, A.; Chaput, L.; Tanaka, I. Distributions of Phonon Lifetimes in Brillouin Zones. *Phys. Rev. B* **2015**, *91*, No. 094306.
(47) Porezag, D.; Pederson, M. R. Infrared Intensities and Raman-Scattering Activities within Density-Functional Theory. *Phys. Rev. B* **1996**, *54*, 7830−7836.
(48) Perdew, J. P.; Burke, K.; Ernzerhof, M. Generalized Gradient Approximation Made Simple. *Phys. Rev. Lett.* **1996**, *77*, 3865−3868.
(49) Jollet, F.; Torrent, M.; Holzwarth, N. Generation of Projector Augmented-Wave Atomic Data: A 71 Element Validated Table in the XML Format. *Comput. Phys. Commun.* **2014**, *185*, 1246−1254.
(50) Momma, K.; Izumi, F. VESTA 3 for three-dimensional visualization of crystal, volumetric and morphology data. *J. Appl. Crystallogr.* **2011**, *44*, 1272−1276.
(51) Rincón, C.; Ramírez, F. J. Lattice Vibrations of $CuInSe_2$ and $CuGaSe_2$ by Raman Microspectrometry. *J. Appl. Phys.* **1992**, *72*, 4321−4324.
(52) Tanino, H.; Maeda, T.; Fujikake, H.; Nakanishi, H.; Endo, S.; Irie, T. Raman Spectra of $CuInSe_2$. *Phys. Rev. B* **1992**, *45*, 13323−13330.
(53) Zaretskaya, E. P.; Gremenok, V. F.; Riede, V.; Schmitz, W.; Bente, K.; Zalesski, V. B.; Ermakov, O. V. Raman Spectroscopy of $CuInSe_2$ Thin Films Prepared by Selenization. *J. Phys. Chem. Solids* **2003**, *64*, 1989−1993.
(54) Witte, W.; Kniese, R.; Powalla, M. Raman Investigations of $Cu(In,Ga)Se_2$ Thin Films with Various Copper Contents. *Thin Solid Films* **2008**, *517*, 867−869.
(55) Chung, C.-H.; Hong, K.-H.; Lee, D.-K.; Yun, J. H.; Yang, Y. Ordered Vacancy Compound Formation by Controlling Element Redistribution in Molecular-Level Precursor Solution Processed $CuInSe_2$ Thin Films. *Chem. Mater.* **2015**, *27*, 7244−7247.
(56) Merino, J. M.; Mahanty, S.; León, M.; Diaz, R.; Rueda, F.; Martin de Vidales, J. L. Structural Characterization of $CuIn_2Se_{3.5}$, $CuIn_3Se_5$ and $CuIn_5Se_8$ Compounds. *Thin Solid Films* **2000**, *361*−*362*, 70−73.
(57) Sobol, P. E.; Nelson, A. J.; Schwerdtfeger, C. R.; Stickle, W. F.; Moulder, J. F. Single Crystal $CuInSe_2$ Analysis by High Resolution XPS. *Surf. Sci. Spectra* **1992**, *1*, 393−397.
(58) Kohiki, S.; Nishitani, M.; Negami, T.; Wada, T. X-Ray Photoelectron Spectroscopy of $CuInSe_2$. *Phys. Rev. B* **1992**, *45*, 9163−9168.
(59) Akhavan, V. A.; Harvey, T. B.; Stolle, C. J.; Ostrowski, D. P.; Glaz, M. S.; Goodfellow, B. W.; Panthani, M. G.; Reid, D. K.; VandenBout, D. A.; Korgel, B. A. Influence of Composition on the Performance of Sintered $Cu(In,Ga)Se_2$ Nanocrystal Thin-Film Photovoltaic Devices. *ChemSusChem* **2013**, *6*, 481−486.
(60) Katari, J. E. B.; Colvin, V. L.; Alivisatos, A. P. X-Ray Photoelectron Spectroscopy of CdSe Nanocrystals with Applications to Studies of the Nanocrystal Surface. *J. Phys. Chem.* **1994**, *98*, 4109−4117.
(61) Schmid, D.; Ruckh, M.; Grunwald, F.; Schock, H. W. Chalcopyrite/Defect Chalcopyrite Heterojunctions on the Basis of $CuInSe_2$. *J. Appl. Phys.* **1993**, *73*, 2902−2909.
(62) Kötschau, I. M.; Schock, H. W. Depth Profile of the Lattice Constant of the Cu-Poor Surface Layer in $(Cu_2Se)_{1-x}(In_2Se_3)_x$ Evidenced by Grazing Incidence X-Ray Diffraction. *J. Phys. Chem. Solids* **2003**, *64*, 1559−1563.
(63) Castle, J.; Chapman-Kpodo, H.; Proctor, A.; Salvi, A. Curve-Fitting in XPS Using Extrinsic and Intrinsic Background Structure. *J. Electron Spectrosc. Relat. Phenom.* **2000**, *106*, 65−80.
(64) Bekenstein, Y.; Vinokurov, K.; Keren-Zur, S.; Hadar, I.; Schilt, Y.; Raviv, U.; Millo, O.; Banin, U. Thermal Doping by Vacancy Formation in Copper Sulfide Nanocrystal Arrays. *Nano Lett.* **2014**, *14*, 1349−1353.
(65) Luther, J. M.; Jain, P. K.; Ewers, T.; Alivisatos, A. P. Localized Surface Plasmon Resonances Arising from Free Carriers in Doped Quantum Dots. *Nat. Mater.* **2011**, *10*, 361−366.
(66) Hessel, C. M.; Pattani, V. P.; Rasch, M.; Panthani, M. G.; Koo, B.; Tunnell, J. W.; Korgel, B. A. Copper Selenide Nanocrystals for Photothermal Therapy. *Nano Lett.* **2011**, *11*, 2560−2566.
(67) Madelung, O. *Semiconductors Data Handbook*; Springer: Berlin, 2013.
(68) Panthani, M. G.; Stolle, C. J.; Reid, D. K.; Rhee, D. J.; Harvey, T. B.; Akhavan, V. A.; Yu, Y.; Korgel, B. A. $CuInSe_2$ Quantum Dot Solar Cells with High Open-Circuit Voltage. *J. Phys. Chem. Lett.* **2013**, *4*, 2030−2034.

DOI: 10.1021/acs.jpcc.9b00558
J. Phys. Chem. C 2019, 123, 9544−9551